Planar Distributed Full-Tensor Anisotropic Metamaterials for Transformation Electromagnetics

Tsutomu Nagayama, *Student Member, IEEE*, and Atsushi Sanada, *Member, IEEE*

***Abstract*—Planar distributed full-tensor anisotropic metamaterials for cloaks of invisibility based on transformation electromagnetics are proposed. The proposed metamaterials are composed of nonresonant transmission lines and are advantageous in full control of the off-diagonal components of the permeability tensor as well as broadband and low-loss characteristics. The explicit design formulas for the metamaterials are given based on the equivalent circuit derived directly from Maxwell's equations. A carpet cloak of invisibility is designed and the validity of the design theory is confirmed by circuit simulations. In addition, the carpet cloak is implemented in microstrip line technology and its performance is demonstrated experimentally at microwave frequencies.**

***Index Terms*—Carpet cloaks of invisibility, metamaterials, transformation electromagnetics.**

I. Introduction

CONCEPTS to realize cloaks of invisibility have been presented based on transformation electromagnetics [1]–[23], surface cloaks [24]–[29], and the like [30]–[33] by using metamaterials composed of small constituents compared with the wavelength of operation.

A cylindrical cloak of invisibility based on the transformation electromagnetics has been implemented by using split-ring resonators (SRRs) and its operation has been first demonstrated at microwave frequencies [3]. However, the cloak exhibits narrow-band and high-loss characteristics due to its intrinsic resonant property. On the other hand, non-resonant wideband and low-loss *carpet cloaks* [5] to conceal an object under the curved reflecting surface have been implemented based on quasi-conformal coordinate transformation [6]–[12]. However, the cloaks cannot fully control the off-diagonal components of the permittivity tensor, and the implementation technique is limited to the quasi-conformal transformation. Therefore, the cloaks can hide only small objects with gentle variation in shape.

In contrast, the transmission-line approach [34]–[38] has been introduced in cloak implementation for easy design feasibility as well as wideband and low-loss characteristics [13]–[17]. The approach has been extended, and equivalent circuit models for full-tensor anisotropic materials are proposed [18]–[20]. The circuit models are the direct projection of Maxwell's equations and provide physical insight and a rigorous design formula with perfect control of anisotropy. The validity of the circuit models has been confirmed by various circuit simulations [18]–[23]. However, the circuit models have not been implemented and their performance has not been experimentally demonstrated so far due to their complex circuit configurations.

In this paper, an implementation method of the equivalent circuit model for full-tensor anisotropic metamaterials based on transformation electromagnetics presented in [20] is proposed. The implemented unit cell is a simple network of transmission-line sections whose characteristic impedances and electrical lengths can be obtained directly from the lumped element values in the original equivalent circuit model without any constraints on individual control of anisotropic tensor parameters. In the following, theory of the implemented distributed anisotropic metamaterial is presented and its performance is demonstrated. In Section II, the circuit model in [20] is first recalled concisely for completion of the paper. In Section III, the proposed distributed anisotropic metamaterials are introduced, and the equivalence of the proposed metamaterials to the circuit model is shown. Rigorous design formulas are also derived theoretically. Then, in order to investigate the validity of the theory, a carpet cloak is designed with the proposed metamaterials in Section IV. In Section V, the operation of the carpet cloak is verified by circuit simulations. Finally, the designed carpet cloak is implemented in microstrip-line technology and its cloaking operation of invisibility is experimentally demonstrated in Section VI.

II. Equivalent Circuit Model

For completion of the paper, we recall the equivalent circuit model presented in [20] which is the basis of the proposed distributed full-tensor anisotropic metamaterials.

Fig. 1 shows the equivalent circuit models for full-tensor anisotropic materials. For simplicity, a square unit cell $\Delta x = \Delta y = \Delta d$ is assumed. Here, x and y branches have the self-inductances $L_x/2$ and $L_y/2$, respectively, and these branches are magnetically coupled with a mutual inductance $M/2$ ($M > 0$ is assumed). Note that Fig. 1(a) and (b) are isomer circuits depending on the magnetic coupling methods between the branches in the x- and y-directions. C is the capacitance to the ground.

Defining the node voltages (V_x, V_{x+1}, V_y, and V_{y+1}) and the currents (I_x, I_y, I_{x+1}, and I_{y+1}) as in Fig. 1, we can obtain the

Manuscript received February 19, 2015; revised May 11, 2015; accepted September 28, 2015. Date of publication November 02, 2015; date of current version December 02, 2015. This work was supported in part by MEXT KAKENHI Grant-in-Aid for Scientific Research on Innovative Areas under Grant 22109002.

The authors are with the Department of Electrical and Electronic Engineering, Yamaguchi University, Yamaguchi 755-8611, Japan (e-mail: t-nagayama@ieee.org; sanada@ieee.org).

Color versions of one or more of the figures in this paper are available online at http://ieeexplore.ieee.org.

Digital Object Identifier 10.1109/TMTT.2015.2487275

0018-9480 © 2015 IEEE. Translations and content mining are permitted for academic research only. Personal use is also permitted, but republication/redistribution requires IEEE permission. See http://www.ieee.org/publications_standards/publications/rights/index.html for more information.

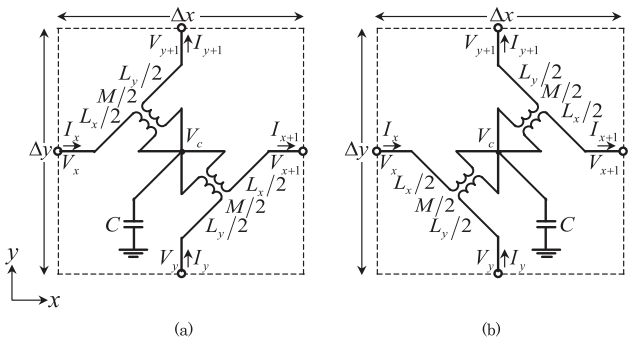

Fig. 1. Equivalent circuit models for full-tensor anisotropic materials [20]. (a) For the $\mu_{xy} = \mu_{yx} > 0$ case. (b) For the $\mu_{xy} = \mu_{yx} < 0$ case.

relation among the currents and the voltages by Kirchhoff's laws. The relations are summarized in the left column in Table I. In the table, ($'$) denotes per-unit-length quantities in the model, i.e., $L'_x = L_x/\Delta d$, $L'_y = L_y/\Delta d$, $M' = M/\Delta d$, and $C' = C/\Delta d$. On the other hand, Maxwell's equations for z-polarized TE waves in an anisotropic material can be written as in the right column in Table I. Comparing these equations with the infinitesimal limit $\Delta d \to 0$, the relations among the circuit parameters and the material parameters are obtained as

$$\begin{pmatrix} L'_y & \pm M' \\ \pm M' & L'_x \end{pmatrix} = \begin{pmatrix} \mu_{xx} & \mu_{xy} \\ \mu_{yx} & \mu_{yy} \end{pmatrix} \tag{1}$$

$$C' = \varepsilon_z. \tag{2}$$

Here, the upper and lower signs of the double signs are for Fig. 1(a) and (b), respectively. These formulas reveal the physical insight of the circuit model, i.e., the diagonal permeability tensor components, μ_{xx} and μ_{yy}, correspond to the self-inductances per-unit-length L'_y and L'_x, respectively, and more importantly, the off-diagonal permeability tensor components, μ_{xy} and μ_{yx}, correspond to the mutual inductance per-unit-length M'. In addition, permittivity ε_z corresponds to the capacitance per-unit-length C'.

III. Proposed Distributed Anisotropic Metamaterials

A. Distributed Anisotropic Metamaterials

In order to implement the anisotropic metamaterial models of Fig. 1(a) and (b), we first rigorously transform the models into Fig. 2(a) and (b) by using a T-circuit expression of an ideal transformer. Then, we introduce the transmission line networks of Fig. 3(a) and (b) by replacing the inductance elements with transmission-line sections. We will refer to these networks as distributed anisotropic metamaterials in the following. Here, Z_{0x}, Z_{0y}, and $Z_{0\mathrm{M}}$ are the characteristic impedances, and $\beta_x l_x$, $\beta_y l_y$, and $\beta_{\mathrm{M}} l_{\mathrm{M}}$ are the electrical lengths of the transmission-line sections (see Fig. 3 for the definition). Obviously, the transmission-line networks in Fig. 3 do not always fully correspond to the equivalent circuits in Fig. 1 just by replacing the inductance elements with the transmission line sections. Therefore, the equivalence will be discussed in the following subsection.

B. Equivalence to the Circuit Model

Let us first consider the Z-parameters of the transmission-line network of Fig. 3(a). Defining the voltage vector as $\boldsymbol{V} = [V_x, V_{x+1}, V_y, V_{y+1}]$ and the current vector as $\boldsymbol{I} = [I_x, -I_{x+1}, I_y, -I_{y+1}]$, we can obtain the Z-parameters

$$\boldsymbol{Z} = (Z_{ij}), \qquad i, j = 1,\ 2,\ 3,\ \text{and}\ 4 \tag{3}$$

theoretically by Kirchhoff's voltage and current laws. Note that all of the directions of the currents in the vector $\boldsymbol{I}$ are defined as the directions flowing into the network. From the network analysis, we can find the following identities:

$$\begin{aligned} Z_{11} &= Z_{22} \\ Z_{33} &= Z_{44} \\ Z_{14} &= Z_{23} = Z_{32} = Z_{41} \\ Z_{12} &= Z_{21} \\ Z_{34} &= Z_{43} \\ Z_{13} &= Z_{24} = Z_{31} = Z_{42}. \end{aligned} \tag{4}$$

$$\tag{5}$$

The concrete formulas for the matrix elements are summarized in the Appendix. On the other hand, obtaining the Z-parameters of the circuit model of Fig. 1(a) as

$$\boldsymbol{Z}' = (Z'_{ij}), \qquad i, j = 1,\ 2,\ 3,\ \text{and}\ 4 \tag{6}$$

we can also find the following identities (see the Appendix):

$$\begin{aligned} Z'_{11} &= Z'_{22} \\ Z'_{33} &= Z'_{44} \\ Z'_{14} &= Z'_{23} = Z'_{32} = Z'_{41} \end{aligned} \tag{7}$$

$$Z'_{12} = Z'_{13} = Z'_{24} = Z'_{34} = Z'_{42} = Z'_{43} = Z'_{21} = Z'_{31}. \tag{8}$$

It is noted that (4) and (7) are consistently equivalent for any network parameters in Fig. 3(a), whereas (5) and (8) are not. However, if the condition

$$\beta_x l_x = \beta_y l_y (\equiv \beta l) \tag{9}$$

is given, all of the parameters in (5) become identical, i.e., $Z_{12} = Z_{13} = Z_{24} = Z_{34} = Z_{42} = Z_{43} = Z_{21} = Z_{31}$, and (5) and (8) become equivalent. In this case, $\boldsymbol{Z} = \boldsymbol{Z}'$ holds, and equivalence of the transmission-line network of Fig. 3(a) to the circuit model of Fig. 1(a) can be guaranteed, i.e., under the condition of (9), the transmission-line network can be definitely expressed by the equivalent circuit model.

Similarly, the equivalence between the other isomer transmission-line network of Fig. 3(b) and the circuit model of Fig. 1(b) can also be shown with the same manner.

C. Design Formula

Under the condition of (9), we can safely obtain the design formulas for determining the transmission-line parameters of the proposed distributed anisotropic metamaterials. By equating

TABLE I
CIRCUIT EQUATIONS AND MAXWELL'S EQUATIONS

Circuit equations	Maxwell's equations
$\left(-\frac{I_{x+1}-I_x}{\Delta d}\right)-\left(\frac{I_{y+1}-I_y}{\Delta d}\right)=j\omega C' V_c$	$\frac{\partial H_y}{\partial x}-\frac{\partial H_x}{\partial y}=j\omega\varepsilon_z E_z$
$\frac{V_{x+1}-V_x}{\Delta d}=\pm j\omega M'\left(\frac{I_{y+1}+I_y}{2}\right)+j\omega L'_x\left(-\frac{I_{x+1}+I_x}{2}\right)$	$\frac{\partial E_z}{\partial x}=j\omega\mu_{yx}H_x+j\omega\mu_{yy}H_y$
$\frac{V_{y+1}-V_y}{\Delta d}=-j\omega L'_y\left(\frac{I_{y+1}+I_y}{2}\right)\mp j\omega M'\left(-\frac{I_{x+1}+I_x}{2}\right)$	$\frac{\partial E_z}{\partial y}=-j\omega\mu_{xx}H_x-j\omega\mu_{xy}H_y$

V_c is the voltage at the center node. μ_{xx}, μ_{xy}, μ_{yx}, and μ_{yy} are permeability tensor components and ε_z is permittivity in the z-direction. The upper and lower signs of the double signs are for Figs. 1(a) and (b), respectively.

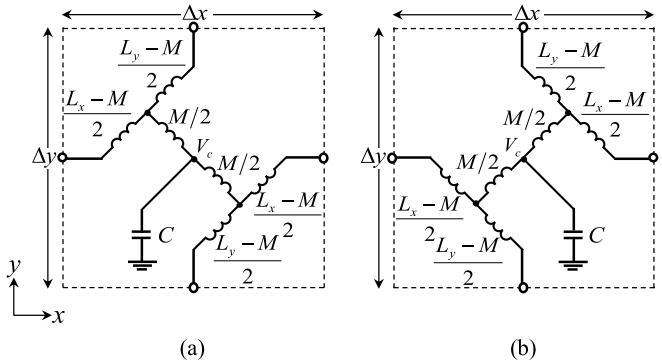

Fig. 2. Transformed equivalent circuits by using T-circuits. (a) For the $\mu_{xy} = \mu_{yx} > 0$ case. (b) For the $\mu_{xy} = \mu_{yx} < 0$ case.

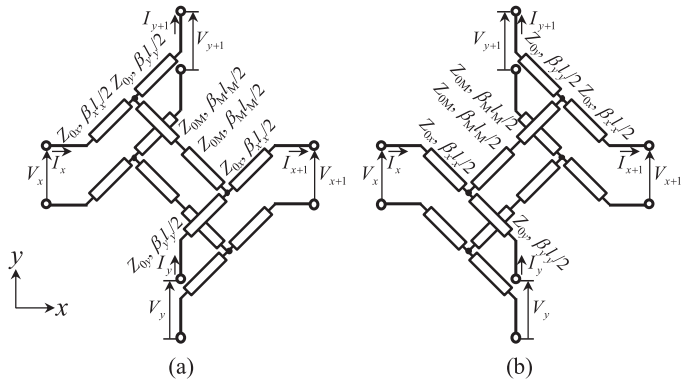

Fig. 3. Proposed distributed anisotropic metamaterials. (a) For the $\mu_{xy} = \mu_{yx} > 0$ case. (b) For the $\mu_{xy} = \mu_{yx} < 0$ case.

(4) to (7) and (5) to (8), the relations between the circuit parameters L_x, L_y, M, and C and the transmission-line parameters Z_{0x}, Z_{0y}, $Z_{0\mathrm{M}}$, βl, and $\beta_{\mathrm{M}} l_{\mathrm{M}}$ can be obtained as

$$L_x - M = \frac{2Z_{0x}}{\omega}\tan\left(\frac{\beta l}{2}\right) \tag{10}$$

$$L_y - M = \frac{2Z_{0y}}{\omega}\tan\left(\frac{\beta l}{2}\right) \tag{11}$$

$$\begin{aligned} M = 2\Bigg[& Z_{0\mathrm{M}}^2 (Y_{0x}+Y_{0y})\tan\left(\frac{\beta l}{2}\right) \\ & + Z_{0\mathrm{M}}\left\{\mathrm{cosec}\,(\beta_{\mathrm{M}} l_{\mathrm{M}}) - \cot(\beta_{\mathrm{M}} l_{\mathrm{M}})\right\}\Bigg] \\ & \Bigg[\omega\Bigg\{\cos^2\left(\frac{\beta l}{2}\right) \\ & + Z_{0\mathrm{M}}(Y_{0x}+Y_{0y})\sin(\beta l)\cot(\beta_{\mathrm{M}} l_{\mathrm{M}}) \\ & - Z_{0\mathrm{M}}^2 (Y_{0x}+Y_{0y})^2 \sin^2\left(\frac{\beta l}{2}\right)\Bigg\}\Bigg] \end{aligned} \tag{12}$$

$$\begin{aligned} C = \frac{1}{\omega}\Bigg\{ & (Y_{0x}+Y_{0y})\sin(\beta l)\cos(\beta_{\mathrm{M}} l_{\mathrm{M}}) \\ & + Y_{0\mathrm{M}}\cos^2\left(\frac{\beta l}{2}\right)\sin(\beta_{\mathrm{M}} l_{\mathrm{M}}) \\ & - Z_{0\mathrm{M}}(Y_{0x}+Y_{0y})^2 \sin^2\left(\frac{\beta l}{2}\right)\sin(\beta_{\mathrm{M}} l_{\mathrm{M}})\Bigg\}. \end{aligned} \tag{13}$$

By solving (10)–(13) simultaneously, the transmission-line parameters of Z_{0x}, Z_{0y}, $Z_{0\mathrm{M}}$, βl, and $\beta_{\mathrm{M}} l_{\mathrm{M}}$ are determined from given circuit parameters of L_x, L_y, M, and C with one degree of freedom, i.e., one of the transmission-line parameters can be chosen arbitrary.

It is noted that these design formulas can be applied to both cases of $\mu_{xy} = \mu_{yx} > 0$ and $\mu_{xy} = \mu_{yx} < 0$ by choosing an appropriate isomer network of either Fig. 3(a) or (b), i.e., if $\mu_{xy} = \mu_{yx} > 0$, Fig. 3(a) with $M = \mu_{xy}\Delta d = \mu_{yx}\Delta d$ (> 0) should be used, and if $\mu_{xy} = \mu_{yx} < 0$, Fig. 3(b) with $M = -\mu_{xy}\Delta d = -\mu_{yx}\Delta d$ (> 0) should be used.

It is also noted that the transmission-line networks in Fig. 3 essentially operate as the lumped element circuits in Fig. 1 at lower frequencies down to dc . For instance, when the frequency approaches to zero in (10), by approximating $\tan x \approx x$, it can be shown that L_x approaches to the frequency independent value as

$$\begin{aligned} L_x - M = \frac{2Z_{0x}}{\omega}\tan\left(\frac{\beta l}{2}\right) &\to \frac{2Z_{0x}}{\omega}\frac{\beta l}{2} = Z_{0x}\frac{\beta l}{\omega} \\ &= \sqrt{\frac{L_{0x}}{C_{0x}}}\sqrt{L_{0x}C_{0x}} \\ &= L_{0x} \end{aligned} \tag{14}$$

where L_{0x} and C_{0x} are the equivalent inductance and capacitance of the transmission line section with the characteristic impedance Z_{0x} in Fig. 3. Similarly, by approximating $\sin x = \tan x \approx x$ and $\cos x \approx 1$ in (11)–(13), it can also be shown that L_y,M, and C approach to frequency independent values as:

$$L_y - M \to L_{0y} \tag{15}$$

$$M \to L_{0\mathrm{M}}\frac{C_{0x}+C_{0y}}{C} \tag{16}$$

$$C \to C_{0x} + C_{0y} + C_{0\mathrm{M}} \tag{17}$$

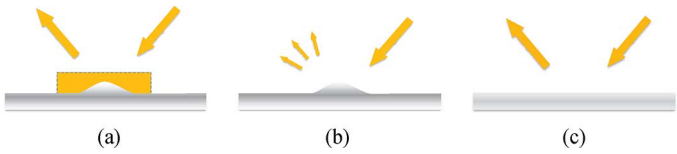

Fig. 4. Concept of a carpet cloak of invisibility. (a) Carpet cloak mimicking specular reflections by a flat floor. (b) Scattering by a bump to be suppressed. (c) Specular reflection by a flat floor to be mimicked.

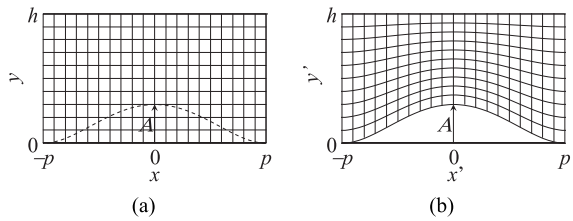

Fig. 5. Coordinate transformation for the carpet cloak design. (a) Original coordinate system. (b) Transformed non-conformal coordinate system.

where (L_{0y}, C_{0y}) and $(L_{0\mathrm{M}}, C_{0\mathrm{M}})$ are the inductance and capacitance values of the corresponding transmission line sections with the characteristic impedance of Z_{0y} and $Z_{0\mathrm{M}}$, respectively, in Fig. 3. Equations (14)–(17) imply that the transmission-line networks in Fig. 3 equivalently operate as the original lumped element circuits in Fig. 1 as the frequency becomes lower. As a result, the bandwidth is limited only by the upper frequency of operation.

IV. Carpet Cloak Design

In order to confirm the validity of the design theory of the proposed distributed anisotropic metamaterials, we design a 2-D carpet cloak of invisibility [5]–[12] hiding objects under the carpet (see Fig. 4). The design consists of two stages: the coordinate transformation determination and the distributed anisotropic metamaterial parameter calculation.

A. Coordinate Transformation

First, we determine an appropriate coordinate transformation. Let us consider the area with height h and width $2p$ shown in Fig. 5(a) including a bump with height A to be hidden. We will now transform the area of Fig. 5(a) in the Cartesian coordinate system (x, y) into the area of Fig. 5(b) in the non-conformal coordinate system (x', y') with the relations

$$x' = x \tag{18}$$

$$y' = y + A\left(1 - \frac{y}{h}\right)\left\{1 - \left(\frac{x}{p}\right)^2\right\}^2 \tag{19}$$

where $-p \le x \le p$ and $0 \le y \le h$, therefore, $-p \le x' \le p$ and $A\{1-(x/p)^2\}^2 \le y' \le h$. In the following, we design the cloak with $p = h$ and $A = 0.3h$.

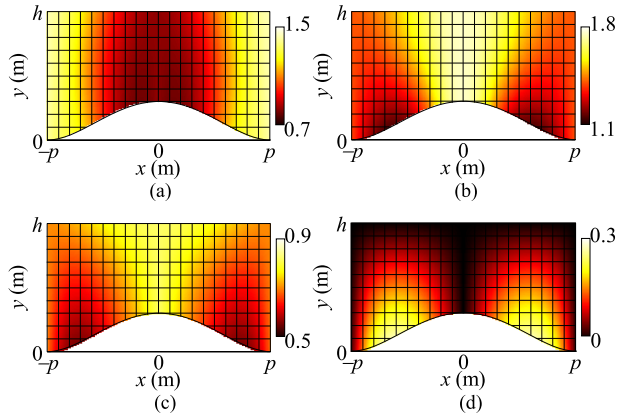

Fig. 6. Transmission-line parameters of the distributed anisotropic metamaterials in Fig. 3 for the carpet cloak design. The unit cell of Fig. 3(a) is used for the half area of $x < 0$, and Fig. 3(b) is used for the half area of $x > 0$. (a) Normalized characteristic impedance Z_{0x}/η. (b) Normalized characteristic impedance Z_{0y}/η. (c) Normalized electrical length $\beta l/k\Delta d$. (d) Normalized electrical length $\beta_{\mathrm{M}} l_{\mathrm{M}}/k\Delta d$.

B. Distributed Anisotropic Metamaterial Parameters

We first calculate the material parameters according to the material interpretation [1], [2], [5], i.e., the coordinate transformation can be mimicked by an inhomogeneous anisotropic material with the tensor parameters

$$\mu^{i'j'} = \left|\det\left(g^{i'j'}\right)\right|^{-1/2} g^{i'j'}\mu \tag{20}$$

$$\varepsilon^{i'j'} = \left|\det\left(g^{i'j'}\right)\right|^{-1/2} g^{i'j'}\varepsilon \tag{21}$$

where μ and ε are the permeability and permittivity of the area to be transformed, and $g^{i'j'}$ is the metric given with the Jacobian transformation matrix $\Lambda_k^{i'}$ as

$$g^{i'j'} = \Lambda_k^{i'}\Lambda_l^{j'}\delta^{kl}. \tag{22}$$

Then, the equivalent circuit parameters L_x, L_y, M, and C in Fig. 1 are readily determined by (1) and (2) as

$$L_x = \mu_{yy}\Delta d \tag{23}$$

$$L_y = \mu_{xx}\Delta d \tag{24}$$

$$M = \pm\,\mu_{xy}\Delta d = \pm\mu_{yx}\Delta d\,(M > 0) \tag{25}$$

$$C = \varepsilon_z \Delta d. \tag{26}$$

Choosing the parameter $Z_{0\mathrm{M}}/\eta = 1.5$ ($\eta = \sqrt{\mu/\varepsilon}$ is the wave impedance in the original area) as a degree of freedom, we determine the other transmission line parameters of Z_{0x}, Z_{0y}, βl, and $\beta_{\mathrm{M}} l_{\mathrm{M}}$ in Fig. 3 from the calculated circuit parameters, L_x, L_y, M, and C by solving (10)–(13) simultaneously. Fig. 6(a) and (b) show obtained Z_{0x} and Z_{0y} normalized by η, and Fig. 6(c) and (d) show βl and $\beta_{\mathrm{M}} l_{\mathrm{M}}$ normalized by $k\Delta d$, respectively, where $k = \omega\sqrt{\varepsilon\mu}$ is the wavenumber in the original area. Here, for the half area of $x < 0$, the unit cell of Fig. 3(a) is used since $\mu_{xy} = \mu_{yx} > 0$ according to (20). Similarly, for the other half area of $x > 0$, Fig. 3(b) is used, since $\mu_{xy} = \mu_{yx} < 0$.

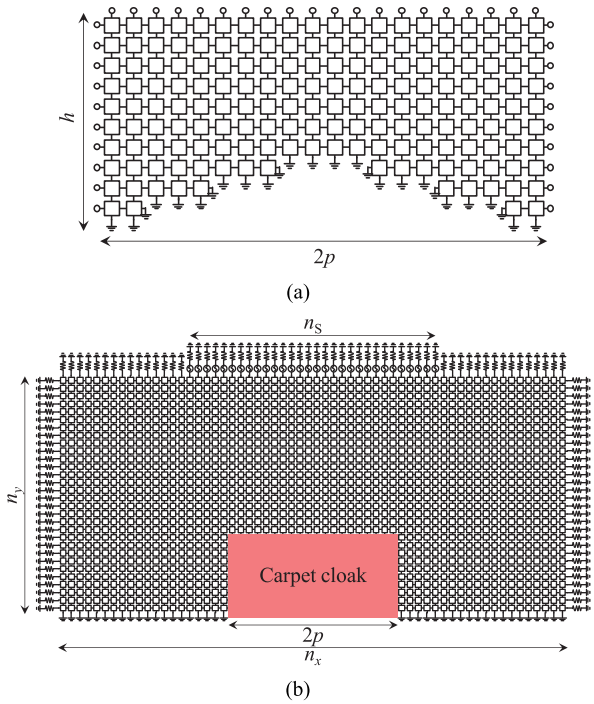

Fig. 7. Configuration of circuit simulations. (a) Cloak area of 20×10 cells ($p = h =$ 50 mm). (b) Configuration for the normal incidence case ($\theta_{\rm inc} =$ 0 deg). The number of cells is $n_x = 300$, $n_y = 150$. Fifty in-phase voltage sources ($n_{\rm s} = 50$) are connected at the nodes in the center of the top row.

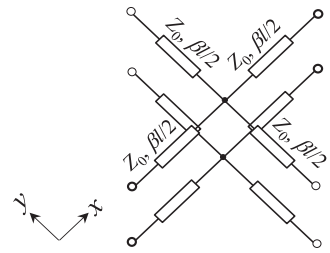

Fig. 8. Unit cell for the isotropic area.

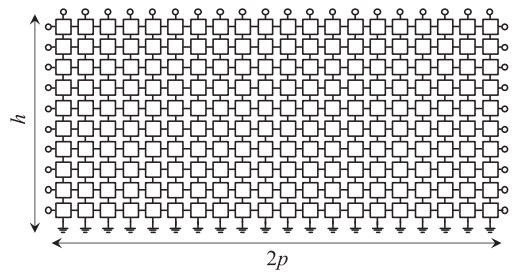

Fig. 9. Isotropic area with 20×10 cells to be placed into the cloak area in Fig. 7(b) for the flat floor simulation.

Incidentally, the permittivity ε_z is implicitly determined by all of the values in Fig. 6.

V. Circuit Simulations

In order to validate the cloak design, circuit simulations are carried out using a SPICE simulator.

We first prepare a node list of 20×10 cells for the cloak area shown in Fig. 7(a). Transmission line parameters for each unit cell are given according to the values in Fig. 6(a)–(d). The transmission line is dealt as an ideal transmission line in the node list. Then, we put the cloak at the bottom center of a uniform isotropic area discretized with $n_x \times n_y = 300 \times 150$ cells as shown in Fig. 7(b). The refractive index and the wave impedance of the isotropic area are chosen to be $n = k/k_0 = 2.14$ (k_0 is the wavenumber in vacuum) and $\eta =$ 63.6 Ω, respectively. In the node list, the outside isotropic area is expressed by the periodic array of the unit cells shown in Fig. 8. The characteristic impedance and the electrical length for both the x- and y-branches are $Z_0 = \sqrt{2}\eta$ and $\beta l = k\Delta d/\sqrt{2}$, respectively, taking into account the effect of 2-D transmission-line networks [35], [36], [38].

Fifty in-phase voltage sources ($n_{\rm s} = 50$) with the internal impedance of 62 Ω,which is reasonably close to the wave impedance $\eta =$ 63.6 Ω,are connected at the nodes in the center of the top row so that the sources illuminate the bump with a normal incident beam ($\theta_{\rm inc} =$ 0 deg). The amplitudes of the voltage sources are set to form the Gaussian beam with the beam waist of $10\Delta d$. Nodes on the bottom boundary of Fig. 7(b) are short-circuited including the bump area. The other nodes on the top row and the side columns are terminated by resistors with 62 Ω that will be used in experiments. The complex voltage distributions of the center nodes in the unit cells are computed in the calculation.

For comparison, two additional simulations are also carried out for: 1) a similar configuration as Fig. 7(b) except for the situation where the cloak area is replaced by a square isotropic area shown in Fig. 9 and 2) another similar configuration as Fig. 7(b) except for the situation where the cloak interior is replaced by isotropic unit cells with the same parameters as those of the outside area. The former corresponds to a simulation for a flat floor, and the latter corresponds to a simulation for a bump without the carpet cloak.

Fig. 10 shows calculated complex voltage distributions for the simulation results for (a) the carpet cloak, (b) a flat floor, and (c) a bump without the carpet cloak. The wavelength is chosen as $\lambda_g = 12\Delta d$ in the calculation. By comparing Fig. 10(a) and (b), it is seen that the carpet cloak mimics the flat floor well. Besides, by comparing Fig. 10(a) and (c), it is clearly seen that scattered waves by the bump are suppressed considerably by the carpet cloak.

Fig. 11(a)–(c) show similar results with the shorter wavelength, $\lambda_g = 6\Delta d$. From these results, it is also seen that the carpet cloak mimics the flat floor, though the level of scattered waves is slightly increased (compare Fig. 11(a) with Fig. 10(a)). Incidentally, it is expected for the cloak to work also at lower frequencies down to DC as discussed in Section III-C.

In order to further confirm the operation of the carpet cloak, circuit simulations with the oblique incident waves $\theta_{\rm inc} = 30$, 45, and 60 deg are carried out. Fig. 12 shows the scheme for the simulations for the case with $\theta_{\rm inc} =$ 45 deg, for instance. In this case, the calculated area is $n_x \times n_y = 300 \times 150$ cells, and a hundred in-phase voltage sources ($n_{\rm s} = 100$) with the Gaussian amplitude distribution are connected at the nodes of the staircase boundary in the top-right corner. For the cases with $\theta_{\rm inc} = 30$ and 60 deg, the calculated areas are chosen as $n_x \times n_y = 172 \times 120$ cells and 240×86 cells, respectively, and the sources are

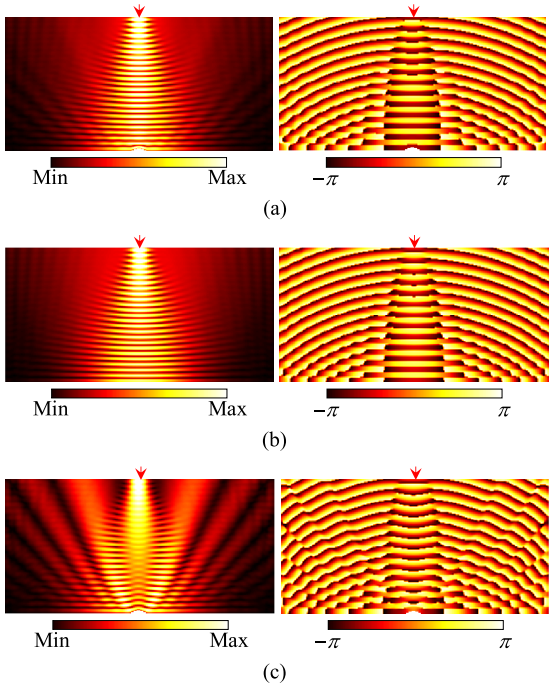

Fig. 10. Calculated complex voltage distributions ($\lambda_g = 12\Delta d$). (a) Carpet cloak. (b) Flat floor. (c) Bump without the carpet cloak. Left: amplitude. Right: phase.

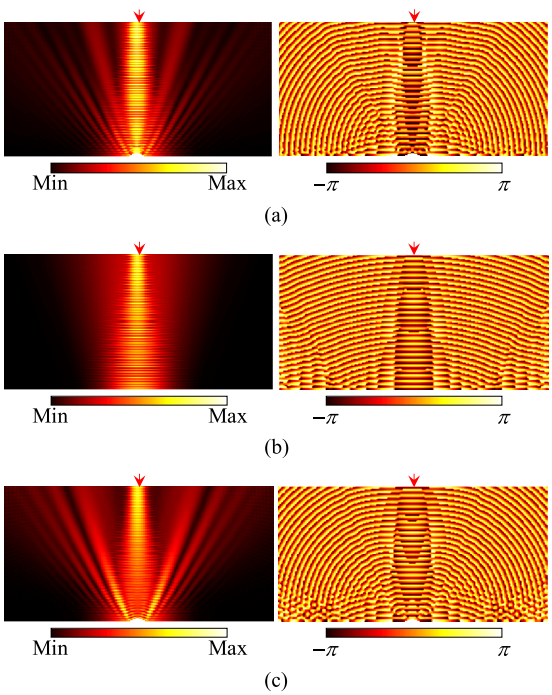

Fig. 11. Calculated complex voltage distributions ($\lambda_g = 6\Delta d$). (a) Carpet cloak. (b) Flat floor. (c) Bump without the carpet cloak. Left: amplitude. Right: phase.

configured with similar staircase approximations to illuminate the cloak centers.

Fig. 13 shows the calculated complex voltage distributions for the cases of (a) $\theta_{\rm inc} = 30$ deg, (b) $\theta_{\rm inc} = 45$ deg, and (c) $\theta_{\rm inc} = 60$ rm deg. In the figure, the cases with the carpet cloak, with a flat floor, and with the bump without the carpet

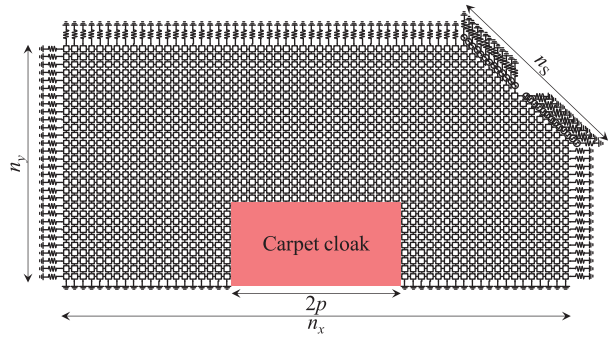

Fig. 12. Configuration of circuit simulations for the oblique incidence case ($\theta_{\rm inc} = 45$ deg). The number of cells is $n_x = 300$, $n_y = 150$. One hundred in-phase voltage sources ($n_{\rm s} = 100$) are connected at the nodes of the staircase boundary in the top-right corner.

cloak are shown from the top to bottom. The wavelength is chosen as $\lambda_g = 12\Delta d$. It is clearly seen from all of these figures that the carpet cloak well suppresses the scattered waves and mimics the flat floor even with the oblique incident angles. From these results, the validity of the design theory is confirmed.

VI. Experiments

Here, the carpet cloak designed in Section IV is implemented with microstrip-line technology, and its cloaking operation of invisibility is verified by near-field measurements.

A. Microstrip-Line Implementation

With the designed transmission line parameters of Fig. 6(a)–(d), the carpet cloak is implemented with microstrip-line technology. The schematics of the anisotropic unit cells for the implementation are shown in Fig. 14. Fig. 14(a) and (b) are for $\mu_{xy} = \mu_{yx} > 0$ and $\mu_{xy} = \mu_{yx} < 0$, respectively. Each of the cells consists of five transmission-line sections of three different kinds of parameters $(\text{width}, \text{length}) = (W_x, l_x)$, (W_y, l_y), and $(W_{\rm M}, l_{\rm M})$. The length of each line section is controlled by the curvature R of the right angle sector. The total lengths l_x, l_y, and $l_{\rm M}$ are defined along the line center. The substrate is backed by a metallic ground plane.

An ARLON DiClad880 with permittivity $\varepsilon_r = 2.17$, thickness $t = 0.254$ mm, and dielectric loss $\tan\delta = 0.00085$ is chosen as a substrate. The width and the height of the cloak area are set to $2p = 100$ mm and $h = 50$ mm, respectively. The cloak is discretized with $\Delta d = 5$ mm. The total number of unit cells in the cloak area is, therefore, 20×10 unit cells. Then, we carefully choose the effective impedance $\eta = 63.6\,\Omega$ and the phase velocity $v_{\rm p} = c_0/n$ (c_0 is the speed of light and $n = 2.14$) of the medium in the original coordinate system to be mimicked considering the fabrication constraints in which the minimum line width is 0.1 mm and all of the lines have to be accommodated in the unit cell. The parameters of W_x, W_y, l_x, l_y, and $l_{\rm M}$ are calculated from the impedances and the electrical lengths of Fig. 6 by assuming $\beta_x/k = \beta_y/k = \beta_{\rm M}/k = 0.615$. Fig. 15(a)–(d) show the calculated W_x, W_y, l_x, l_y and $l_{\rm M}$. Here, for the half areas of $x < 0$ and $x > 0$, the

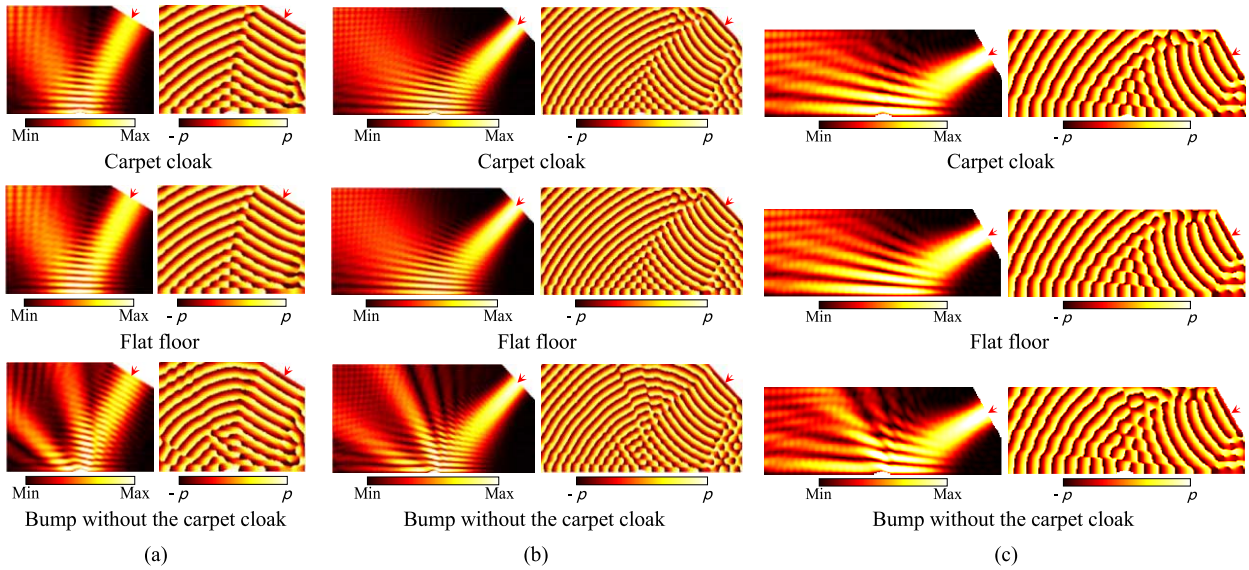

Fig. 13. Calculated complex voltage distributions for oblique incidence cases ($\lambda_g = 12\Delta d$). (a) $\theta_{\rm inc} = 30$ deg. (b) $\theta_{\rm inc} = 45$ deg. (c) $\theta_{\rm inc} = 60$ deg. Left: Amplitude. Right: Phase.

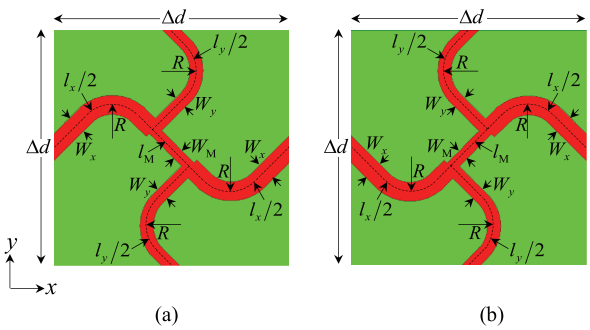

Fig. 14. Schematics of the unit cells of the anisotropic metamaterials implemented on a dielectric substrate with the microstrip-line technology. (a) For the $\mu_{xy} = \mu_{yx} > 0$ case. (b) For the $\mu_{xy} = \mu_{yx} < 0$ case.

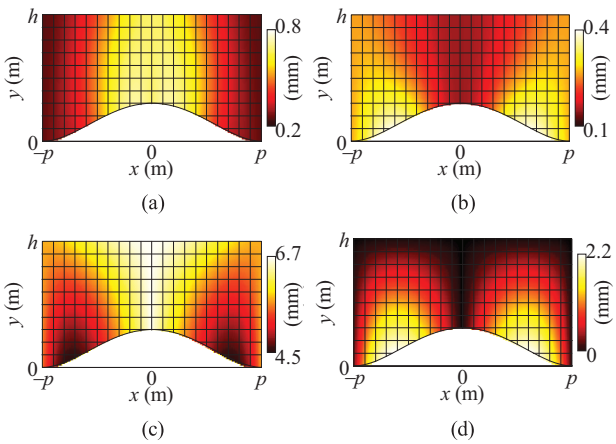

Fig. 15. Line widths and lengths of the implemented anisotropic unit cells in Fig. 14 for the carpet cloak design. The unit cell of Fig. 14(a) is used for the half area of $x < 0$, and Fig. 14(b) is used for the half area of $x > 0$. (a) Line width W_x. (b) Line width W_y. (c) Line length $l_x = l_y$. (d) Line length $l_{\rm M}$.

unit cells of Fig. 14(a) and (b) are used, respectively. The parameter $W_{\rm M} = 0.231$ mm is determined from $Z_{0\rm M} = 1.5\eta$.

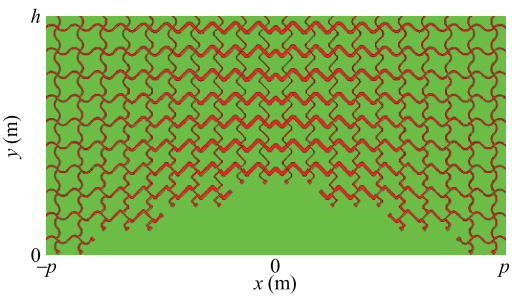

Fig. 16. Implemented carpet cloak.

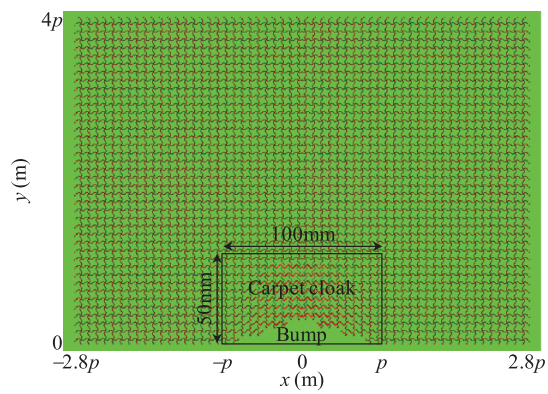

Fig. 17. Schematic for the prototype.

Fig. 16 shows the implemented carpet cloak. As seen in Fig. 16, the cloak is symmetrical with the center of $x = 0$. At the interface on $x = 0$, the branches of the unit cells are connected smoothly maintaining the electrical length.

B. Prototypes

Fig. 17 shows the schematic of the carpet cloak for fabrication. The carpet cloak area designed in Fig. 16 is placed at the bottom center of a uniform isotropic area consisting of an array

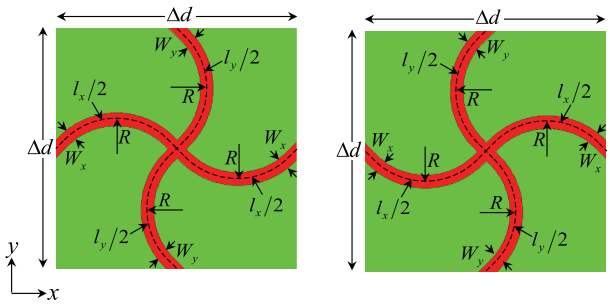

Fig. 18. Unit cells of the isotropic area outside of the cloak area. (a) For the left-half area of Fig. 17. (b) For the right-half area of Fig. 17.

of unit cells shown in Fig. 18. Although Fig. 18(a) and (b) are electrically identical, they are used in the left- and right-half of the isotropic area, respectively, to match the cloak geometry. The unit cell parameters for the outside isotropic area are chosen as $W_x = W_y = 0.264$ mm and $l(= l_x = l_y) = 5.75$ mm to have the refractive index of $n = 2.14$ and the wave impedance of $\eta = 63.6\ \Omega$. The total area of Fig. 17 is 280×200 mm^2 ($n_x \times n_y = 56 \times 40$ cells).

Fig. 19(a) shows the fabricated prototype for the carpet cloak. For comparison, another two prototypes with a flat floor [Fig. 19(b)] and with a bump without the carpet cloak [Fig. 19(c)] are also fabricated, as introduced in the simulations in Section V.

For all the prototypes in Fig. 19, the nodes on the bottom boundary including the bump area is short-circuited by through-hole vias with the diameter of $\phi = 0.3$ mm. The other boundaries are terminated by chip resistors with 62 Ω through metallic lands with 0.8×0.5 mm^2.

C. Measurement System

Fig. 20 shows the near-field measurement system used in the experiments. A prototype is fixed with an adhesive sheet on an aluminum plate to avoid warp. The prototype is excited by a coaxial cable soldered at the center node on the top row, and distributions of the z-component of the electric near-field approximately 0.5 mm above the prototype surface are measured by using a coaxial probe with a computer controlled xyz-stage. The total measured area is 275×190 mm^2. The complex electric field data are acquired in every 1.25 mm both in the x- and y-directions, and the total number of the measurement points is 221×153. In order to suppress the direct coupling between the excitation coaxial cable and the electric probe, the differential measurement technique is used, in which the complex field distributions on two slightly different planes are differentiated. The distance between the two planes is chosen as 1.5 mm.

D. Measured Near-Field Distributions

Fig. 21 shows the measured amplitude and phase distributions at 2.20 GHz ($\lambda_g = 12.7\Delta d$) for (a) the carpet cloak, (b) a flat floor, and (c) a bump without the carpet cloak. It is seen from Fig. 21(a) for the carpet cloak that the wave front of the reflected wave by the cloak is flattened outside the cloak area

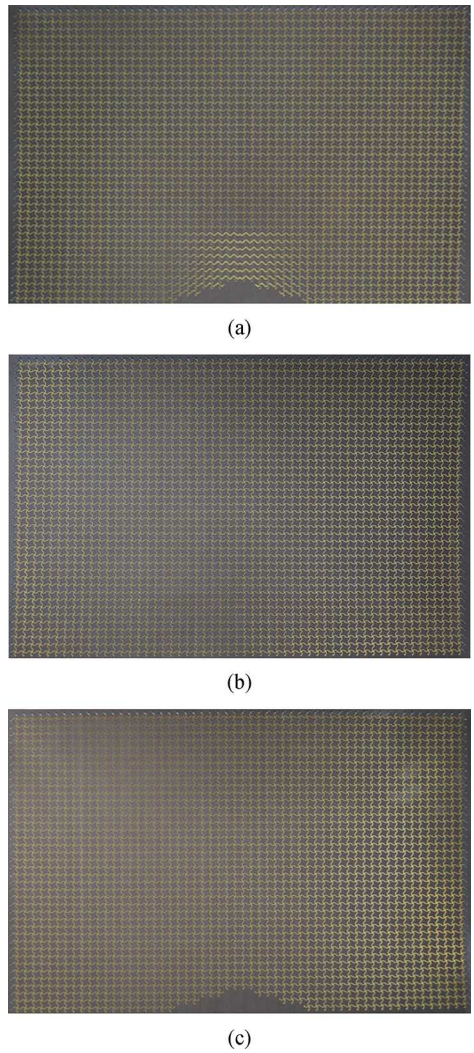

Fig. 19. Prototypes. (a) Carpet cloak. (b) Flat floor. (c) Bump without the carpet cloak.

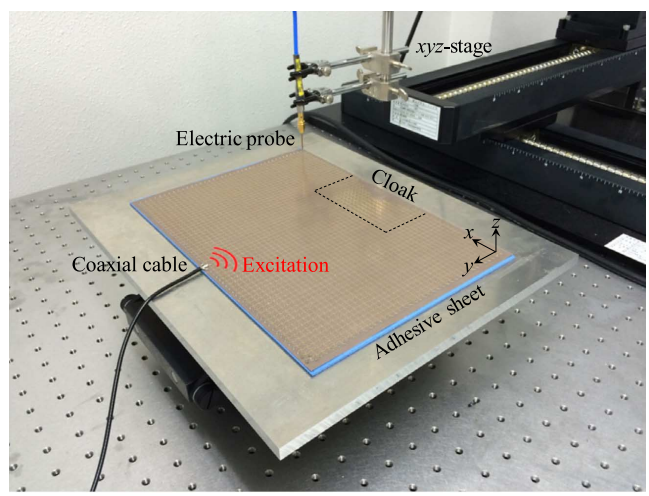

Fig. 20. Near-field measurement system.

and the total field distribution reflects well the scattered field by the flat floor shown in Fig. 21(b). In contrast, in Fig. 21(c) for a bump without the coordinate transformation, the incident wave

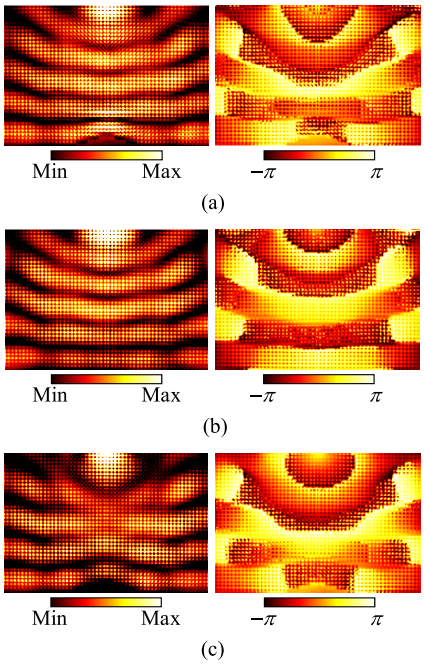

Fig. 21. Measured complex electric near-field distributions ($\lambda_g = 12.7\Delta d$ at 2.20 GHz). (a) Carpet cloak. (b) Flat floor. (c) Bump without the carpet cloak. Left: amplitude. Right: phase.

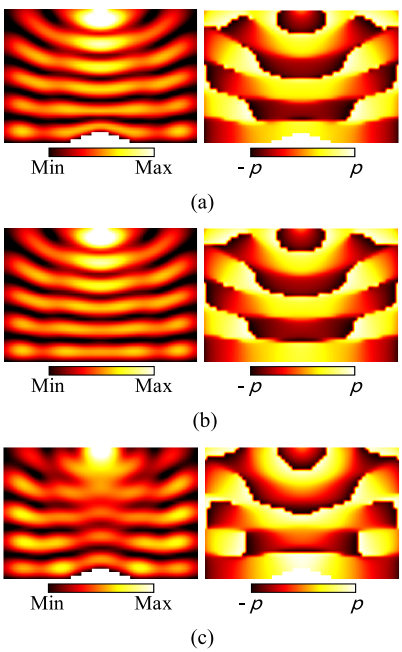

Fig. 22. Calculated complex voltage distributions ($\lambda_g = 12.7\Delta d$ at 2.20 GHz). (a) Carpet cloak. (b) Flat floor. (c) Bump without the carpet cloak. Left: amplitude. Right: phase.

is scattered by the bump to the left and right and the wave front is bent according to the bump shape.

For comparison, circuit simulations for the same configurations as the experiments are carried out with the same manner as in Section V. The results for (a) the carpet cloak, (b) a flat floor, and (c) a bump without the carpet cloak are shown in Fig. 22. By comparing Fig. 22 with the measured results of Fig. 21, they

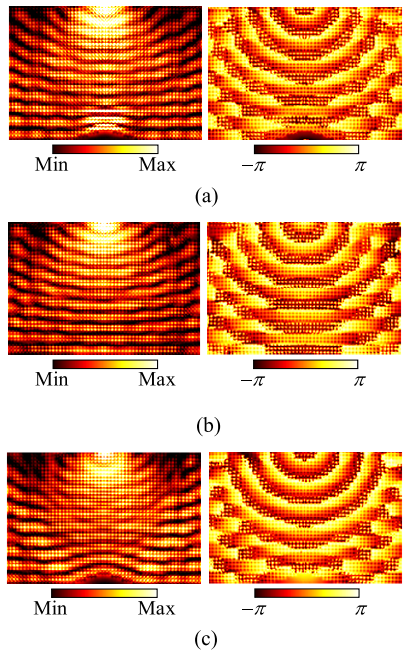

Fig. 23. Measured complex electric near-field distributions ($\lambda_g = 6.2\Delta d$ at 4.55 GHz). (a) Carpet cloak. (b) Flat floor. (c) Bump without the carpet cloak. Left: amplitude. Right: phase.

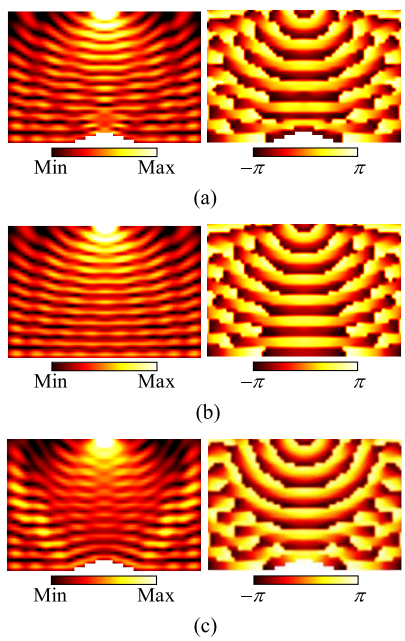

Fig. 24. Calculated complex voltage distributions ($\lambda_g = 6.2\Delta d$ at 4.55 GHz). (a) Carpet cloak. (b) Flat floor. (c) Bump without the carpet cloak. Left: Amplitude. Right: Phase.

agree well with each other reflecting the fact that the carpet cloak well suppresses the scattered waves by the bump.

Fig. 23 shows measured electric field distributions at a higher frequency 4.55 GHz ($\lambda_g = 6.2\Delta d$) for (a) the carpet cloak, (b) a flat floor, and (c) a bump without the carpet cloak. By comparing Fig. 23(a) and (b), it is seen that the carpet cloak sufficiently suppresses the scattered waves by the bump and mimics the flat floor. In contrast, in Fig. 23(c), it is clearly seen that the incident wave is strongly scattered by the bump in the oblique

directions with the angles of approximately ± 30 deg, which is distinct from Fig. 23(a) for the case with the carpet cloak.

Fig. 24 shows similar circuit simulation results at 4.55 GHz ($\lambda_g = 6.2\Delta d$) for (a) the carpet cloak, (b) a flat floor, and (c) a bump without the carpet cloak. It is seen from the figure that the simulated results agree well with the corresponding measured results in Fig. 23(a)–(c), and the validity of the measured results are confirmed.

From these results, it can be concluded that the validity of the theory of the proposed distributed full-tensor anisotropic metamaterials as well as the operations of the carpet cloak are confirmed experimentally.

VII. Conclusion

Distributed full-tensor anisotropic metamaterials for transformation electromagnetics have been proposed. First, equivalence of the proposed metamaterials to the circuit models for the full-tensor anisotropic material has been shown, and the design formulas have been derived. Then, a carpet cloak has been designed. Circuit simulations have revealed the validity of the design as well as the broadband operation. In addition, the designed carpet cloak has been implemented on a dielectric substrate with microstrip-line technology. By the near-field measurements, it has been experimentally shown that the carpet cloak well suppresses scattered waves by the bump and mimics the flat floor. Therefore, the validity of the theory of the proposed distributed full-tensor anisotropic metamaterials has been confirmed.

This approach can be useful for implementing novel planar circuit devices based on the transformation electromagnetics. For instance, the idea can be applied to a coordinate transformed 2-D resonator whose resonant frequencies are exactly the same as those of the original resonator including higher harmonics regardless of its physical shape. The concept and implementation could also be exploited to Rotman lenses or other novel devices and circuits based on 2-D wave propagation.

Although the proposed implementation method is limited to 2-D cases, 3-D extensions will be demanded for the next stage. A possible approach is extending the proposed transmission line network in the symmetrical condensed node presented in the 3-D TLM approach.

Appendix

The Z-parameter components of (3) for the transmission-line network in Fig. 3(a) are given as

$$\begin{aligned} Z_{11} &= Z_{22} \\ &= jZ_{0x}\tan\left(\frac{\beta_x l_x}{2}\right) \\ &\quad + \frac{1}{D}\left[j\frac{Z_{0\mathrm{M}}^2}{Z_{0x}}\left\{\tan\left(\frac{\beta_x l_x}{2}\right)+\tan^3\left(\frac{\beta_x l_x}{2}\right)\right\}\right. \\ &\qquad + j\frac{Z_{0\mathrm{M}}^2}{Z_{0y}}\sec^2\left(\frac{\beta_x l_x}{2}\right)\tan\left(\frac{\beta_y l_y}{2}\right) \\ &\qquad \left. -jZ_{0\mathrm{M}}^2\sec^2\left(\frac{\beta_x l_x}{2}\right)\cot\left(\beta_{\mathrm{M}} l_{\mathrm{M}}\right)\right] \end{aligned} \tag{A1}$$

and

$$\begin{aligned} Z_{33} &= Z_{44} = jZ_{0y}\tan\left(\frac{\beta_y l_y}{2}\right) \\ &\quad + \frac{1}{D}\left[j\frac{Z_{0\mathrm{M}}^2}{Z_{0x}}\tan\left(\frac{\beta_x l_x}{2}\right)\sec^2\left(\frac{\beta_y l_y}{2}\right)\right. \\ &\qquad + j\frac{Z_{0\mathrm{M}}^2}{Z_{0y}}\left\{\tan\left(\frac{\beta_y l_y}{2}\right)+\tan^3\left(\frac{\beta_y l_y}{2}\right)\right\} \\ &\qquad \left. -jZ_{0\mathrm{M}}^2\sec^2\left(\frac{\beta_y l_y}{2}\right)\cot\left(\beta_{\mathrm{M}} l_{\mathrm{M}}\right)\right] \end{aligned} \tag{A2}$$

$$\begin{aligned} Z_{14} &= Z_{23} = Z_{32} = Z_{41} \\ &= \frac{1}{D}\left[j\frac{Z_{0\mathrm{M}}^2}{Z_{0x}}\tan\left(\frac{\beta_x l_x}{2}\right)\sec\left(\frac{\beta_x l_x}{2}\right)\sec\left(\frac{\beta_y l_y}{2}\right)\right. \\ &\quad + j\frac{Z_{0\mathrm{M}}^2}{Z_{0y}}\sec\left(\frac{\beta_x l_x}{2}\right)\tan\left(\frac{\beta_y l_y}{2}\right)\sec\left(\frac{\beta_y l_y}{2}\right) \\ &\quad \left. -jZ_{0\mathrm{M}}\sec\left(\frac{\beta_x l_x}{2}\right)\sec\left(\frac{\beta_y l_y}{2}\right)\cot\left(\beta_{\mathrm{M}} l_{\mathrm{M}}\right)\right] \end{aligned} \tag{A3}$$

$$Z_{12} = Z_{21} = \frac{1}{D}\left[-jZ_{0\mathrm{M}}\sec^2\left(\frac{\beta_x l_x}{2}\right)\mathrm{cosec}\left(\beta_{\mathrm{M}} l_{\mathrm{M}}\right)\right] \tag{A4}$$

$$Z_{34} = Z_{43} = \frac{1}{D}\left[-jZ_{0\mathrm{M}}\sec^2\left(\frac{\beta_y l_y}{2}\right)\mathrm{cosec}\left(\beta_{\mathrm{M}} l_{\mathrm{M}}\right)\right] \tag{A5}$$

$$\begin{aligned} Z_{13} &= Z_{24} = Z_{31} = Z_{42} \\ &= \frac{1}{D}\left[-jZ_{0\mathrm{M}}\sec\left(\frac{\beta_x l_x}{2}\right)\sec\left(\frac{\beta_y l_y}{2}\right)\mathrm{cosec}\left(\beta_{\mathrm{M}} l_{\mathrm{M}}\right)\right] \end{aligned} \tag{A6}$$

where

$$\begin{aligned} D &= 2\cot\left(\beta_{\mathrm{M}} l_{\mathrm{M}}\right)\left\{\frac{Z_{0\mathrm{M}}}{Z_{0x}\cot\left(\frac{\beta_x l_x}{2}\right)}+\frac{Z_{0\mathrm{M}}}{Z_{0y}\cot\left(\frac{\beta_y l_y}{2}\right)}\right\}+1 \\ &\quad -\cot\left(\beta_{\mathrm{M}} l_{\mathrm{M}}\right)\left\{\frac{Z_{0\mathrm{M}}}{Z_{0x}\cot\left(\frac{\beta_x l_x}{2}\right)}+\frac{Z_{0\mathrm{M}}}{Z_{0y}\cot\left(\frac{\beta_y l_y}{2}\right)}\right\}^2. \end{aligned} \tag{A7}$$

The Z-parameter components of (6) for the equivalent circuit model in Fig. 1(a) are given as

$$Z'_{11} = Z'_{22} = \frac{j\omega L_x}{2} + \frac{1}{j\omega C} \tag{A8}$$

$$Z'_{33} = Z'_{44} = \frac{j\omega L_y}{2} + \frac{1}{j\omega C} \tag{A9}$$

$$Z'_{14} = Z'_{23} = Z'_{32} = Z'_{41} = \frac{j\omega M}{2} + \frac{1}{j\omega C} \tag{A10}$$

$$Z'_{12} = Z'_{13} = Z'_{21} = Z'_{24} = Z'_{31} = Z'_{34} = Z'_{42} = Z'_{43} = \frac{1}{j\omega C}. \tag{A11}$$

References

[1] J. B. Pendry, D. Schurig, and D. R. Smith, "Controlling electromagnetic fields," *Science*, vol. 312, no. 5781, pp. 1780–1782, Jun. 2006.

[2] D. Schurig, J. B. Pendry, and D. R. Smith, "Calculation of material properties and ray tracing in transformation media," *Opt. Exp.*, vol. 14, no. 21, pp. 9794–9804, Oct. 2006.

[3] D. Schurig, J. J. Mock, B. J. Justice, S. A. Cummer, J. B. Pendry, A. F. Starr, and D. R. Smith, "Metamaterial electromagnetic cloak at microwave frequencies," *Science*, vol. 314, no. 5801, pp. 977–980, Nov. 2006.
[4] B. Kanté, D. Germain, and A. de Lustrac, "Experimental demonstration of a nonmagnetic metamaterial cloak at microwave frequencies," *Phys. Rev. B.*, vol. 80, no. 20, Nov. 2009, Art. ID 201104.
[5] J. Li and J. B. Pendry, "Hiding under the carpet: A new strategy for cloaking," *Phys. Rev. Lett.*, vol. 101, no. 20, Nov. 2008, Art. ID 203901.
[6] J. Valentine, J. Li, T. Zentgraf, G. Bartal, and X. Zhang, "An optical cloak made of dielectrics," *Nature Mater.*, vol. 8, pp. 568–571, Apr. 2009.
[7] R. Liu, C. Ji, J. J. Mock, J. Y. Chin, T. J. Cui, and D. R. Smith, "Broadband ground-plane cloak," *Science*, vol. 323, no. 5912, pp. 366–369, Jan. 2009.
[8] J. H. Lee, J. Blair, V. A. Tamma, Q. Wu, S. J. Rhee, C. J. Summers, and W. Park, "Direct visualization of optical frequency invisibility cloak based on silicon nanorod array," *Opt. Exp.*, vol. 17, no. 15, pp. 12922–12928, Jul. 2009.
[9] L. H. Gabrielli, J. Cardenas, C. B. Poitras, and M. Lipson, "Silicon nanostructure cloak operating at optical frequencies," *Nature Photon.*, vol. 3, pp. 461–463, Aug. 2009.
[10] T. Ergin, N. Stenger, P. Brenner, J. B. Pendry, and M. Wegener, "Three-dimensional invisibility cloak at optical wavelengths," *Science*, vol. 328, no. 5976, pp. 337–339, Apr. 2010.
[11] H. F. Ma and T. J. Cui, "Three-dimensional broadband ground-plane cloak made of metamaterials," *Nature Commun.*, vol. 1, p. 21, Feb. 2011.
[12] D. Shin, Y. Urzhumov, Y. Jung, G. Kang, S. Baek, M. Choi, H. Park, K. Kim, and D. R. Smith, "Broadband electromagnetic cloaking with smart metamaterials," *Nature Commun.*, vol. 3, p. 1213, Nov. 2012.
[13] P. Alitalo, O. Luukkonen, L. Jylhä, J. Venermo, and S. Tretyakov, "Transmission-line networks cloaking objects from electromagnetic fields," *IEEE Trans. Antennas Propagat.*, vol. 56, no. 2, pp. 416–424, Feb. 2008.
[14] P. Alitalo and S. Tretyakov, "Broadband microwave cloaking with periodic networks of transmission lines," in *Proc. Metamaterials*, Sep. 2008, pp. 392–394.
[15] P. Alitalo, F. Bongard, J.-F. Zürcher, J. Mosig, and S. Tretyakov, "Experimental verification of broadband cloaking using a volumetric cloak composed of periodically stacked cylindrical transmission-line networks," *Appl. Phys. Lett.*, vol. 94, no. 1, Jan. 2009, Art. ID 014103.
[16] P. Alitalo, F. Bongard, J.-F. Zürcher, J. Mosig, and S. Tretyakov, "Broadband electromagnetic cloaking of long cylindrical objects," *Phys. Rev. Lett.*, vol. 103, no. 10, Sep. 2009, Art. ID 103905.
[17] X. Liu, C. Li, K. Yao, X. Meng, W. Feng, B. Wu, and F. Li, "Experimental verification of broadband invisibility using a cloak based on inductor-capacitor networks," *Appl. Phys. Lett.*, vol. 95, no. 19, Nov. 2009, Art. ID 191107.
[18] M. Zedler and G. V. Eleftheriades, "2D transformation optics using anisotropic transmission-line metamaterials," in *IEEE MTT-S Int. Microw. Symp. Dig.*, May 2010, pp. 33–36.
[19] A. Sanada and T. Nagayama, "Transmission line approach for transformation electromagnetics," in *Proc. URSI Int. Symp. Electromagn. Theory*, May 2013, pp. 336–337.
[20] T. Nagayama and A. Sanada, "Physical equivalent circuit model for 2D full-tensor anisotropic metamaterials," in *IEEE MTT-S Int. Microw. Symp. Dig.*, Jun. 2013, pp. 1–3.
[21] T. Nagayama and A. Sanada, "Specular reflection from a sinusoidal periodic boundary by a carpet cloak of invisibility," in *Proc. Asia–Pacific Microw, Conf.*, Nov. 2013, pp. 1209–1211.
[22] A. Sanada and T. Nagayama, "Transmission line approach to 2D full-tensor anisotropic metamaterials for transformation electromagnetics," in *Proc. Int. Conf. Electromagn. Advanced Appl.*, Aug. 2014, pp. 804–805.
[23] A. Sanada and T. Nagayama, "Transmission line metamaterials for transformation electromagnetics," in *Proc. Eur. Microw. Conf.*, Oct. 2014, pp. 965–967.
[24] A. Alù, "Mantle cloak: Invisibility induced by a surface," *Phys. Rev. B.*, vol. 80, no. 24, Oct. 2009, Art. ID 245115.
[25] Y. R. Padooru, A. B. Yakovlev, P.-Y. Chen, and A. Alù, "Analytical modeling of conformal mantle cloaks for cylindrical objects using subwavelength printed and slotted arrays," *Appl. Phys. Lett.*, vol. 112, no. 3, Aug. 2012, Art. ID 034907.
[26] M. Selvanayagam and G. Eleftheriades, "An active electromagnetic cloak based on the equivalence principle," *IEEE Antennas Microw. Wireless Propag. Lett.*, vol. 11, no. 10, pp. 1226–1229, Oct. 2012.
[27] M. Selvanayagam and G. Eleftheriades, "Discontinuous electromagnetic fields using orthogonal electric and magnetic currents for wavefront manipulation," *Opt. Exp.*, vol. 21, no. 12, pp. 14409–14429, Jun. 2013.
[28] M. Selvanayagam and G. Eleftheriades, "Experimental demonstration of active electromagnetic cloaking," *Phys. Rev. X*, vol. 3, no. 4, Jun. 2013, Art. ID 041011.
[29] R. S. Schofield, J. C. Soric, D. Rainwater, A. Kerkhoff, and A. Alù, "Scattering suppression and wideband tenability of a flexible mantle cloak for finite-length conducting rods," *New J. Phys.*, vol. 16, no. 6, Jun. 2014, Art. ID 063063.
[30] U. Leonhardt, "Optical conformal mapping," *Science*, vol. 312, no. 5781, pp. 1777–1780, Jun. 2006.
[31] M. G. Silveirinha, A. Alù, and N. Engheta, "Parallel-plate metamaterials for cloaking structures," *Phys. Rev. E*, vol. 75, no. 3, Mar. 2007, Art. ID 036603.
[32] B. Edwards, A. Alù, M. G. Silveirinha, and N. Engheta, "Experimental verification of plasmonic cloaking at microwave frequencies with metamaterials," *Phys. Rev. Lett.*, vol. 103, no. 15, Oct. 2009, Art. ID 153901.
[33] R. Schittny, M. Kadie, T. Biickmann, and M. Wegener, "Invisibility cloaking in a diffusive light scattering medium," *Science*, vol. 345, no. 6195, pp. 427–429, Jul. 2014.
[34] G. Kron, "Equivalent circuit of the field equations of Maxwell-I," *Proc. IRE*, vol. 32, no. 5, pp. 289–299, May 1944.
[35] P. B. Johns and R. L. Beurle, "Numerical solution of 2-dimensional scattering problems using a transmission-line matrix," *Proc. Inst. Electr. Eng.*, vol. 118, no. 9, pp. 1203–1208, Sep. 1971.
[36] W. J. R. Hoefer, "The transmission-line matrix method–theory and applications," *IEEE Trans. Microw. Theory Techn.*, vol. MTT-33, no. 10, pp. 882–893, Oct. 1985.
[37] P. B. Johns, "A symmetrical condensed node for the TLM method," *IEEE Trans. Microw. Theory Techn.*, vol. MTT-35, no. 4, pp. 370–377, Apr. 1987.
[38] C. Christopoulos, *The Transmission-Line Modeling Method: TLM*. New York, NY, USA: IEEE, 1995.

Tsutomu Nagayama (S'13) received the B. E. and M. E. degrees in electrical and electronics engineering from Yamaguchi University, Yamaguchi, Japan, in 2011 and 2013, respectively, where he is currently working toward the Ph.D. degree at the Graduate School of Science and Engineering.

His research is concerned with transformation electromagnetics and metamaterials.

Mr. Nagayama is a student member of the Institute of Electronics, Information and Communication Engineers (IEICE).

Atsushi Sanada (M'95) received the B. E., M.E., and Ph.D. degrees in electrical engineering from Okayama University, Okayama, Japan, in 1989, 1991, and 1994, respectively.

In 1999, he joined the Faculty of Engineering, Yamaguchi University, Yamaguchi, Japan, where he is now a Professor. He was a Visiting Scholar with the University of California at Los Angeles in 1994–1995 and 2002–2003. He was also a Visiting Scholar with the Advanced Telecommunications Research Institute International in 2004–2005 and the Japan Broadcasting Corporation in 2005. His research is concerned with material science and technologies including transformation electromagnetics and metamaterials, high-T_c superconducting and magnetic materials.

Dr. Sanada is a member of the European Microwave Association (EuMA) and the Institute of Electronics, Information and Communication Engineers (IEICE). He is currently serving as an IEEE Microwave Theory and Techniques Society (MTT-S) AdCom member.